# First results from the GlueX experiment

Cite as: AIP Conference Proceedings **1735**, 020001 (2016); https://doi.org/10.1063/1.4949369
Published Online: 25 May 2016

**The GlueX Collaboration, H. Al Ghoul, E. G. Anassontzis, et al.**



# First Results from The GlueX Experiment

The GlueX Collaboration, H. Al Ghoul[7], E. G. Anassontzis[2], F. Barbosa[11], A. Barnes[5], T. D. Beattie[19], D. W. Bennett[10], V. V. Berdnikov[12], T. Black[17], W. Boeglin[6], W. K. Brooks[20], B. Cannon[7], O. Chernyshov[9], E. Chudakov[11], V. Crede[7], M. M. Dalton[11], A. Deur[11], S. Dobbs[18], A. Dolgolenko[9], M. Dugger[1], H. Egiyan[11], P. Eugenio[7], A. M. Foda[19], J. Frye[10], S. Furletov[11], L. Gan[17], A. Gasparian[16], A. Gerasimov[9], N. Gevorgyan[21], V. S. Goryachev[9], B. Guegan[14], L. Guo[6], H. Hakobyan[20], H. Hakobyan[21], J. Hardin[14], G. M. Huber[19], D. Ireland[8], M. M. Ito[11], N. S. Jarvis[3], R. T. Jones[5], V. Kakoyan[21], M. Kamel[6], F. J. Klein[4], C. Kourkoumeli[2], S. Kuleshov[20], M. Lara[10], I. Larin[9], D. Lawrence[11], J. Leckey[10], W. I. Levine[3], K. Livingston[8], G. J. Lolos[19], D. Mack[11], P. T. Mattione[11], V. Matveev[9], M. McCaughan[11], W. McGinley[3], J. McIntyre[5], R. Mendez[20], C. A. Meyer[3,a)], R. Miskimen[13], R. E. Mitchell[10], F. Mokaya[5], K. Moriya[1], G. Nigmatkulov[12], N. Ochoa[19], A. I. Ostrovidov[7], Z. Papandreou[19], R. Pedroni[16], M. Pennington[11], L. Pentchev[11], A. Ponosov[12], E. Pooser[6], B. Pratt[5], Y. Qiang[11], J. Reinhold[6], B. G. Ritchie[1], L. Robison[18], D. Romanov[12], C. Salgado[15], R. A. Schumacher[3], A. Yu. Semenov[19], I. A. Semenova[19], I. Senderovich[1], K. K. Seth[18], M. R. Shepherd[10], E. S. Smith[11], D. I. Sober[4], A. Somov[11], S. Somov[12], O. Soto[20], N. Sparks[4], M. J. Staib[3], J. R. Stevens[11], A. Subedi[10], V. Tarasov[9], S. Taylor[11], I. Tolstukhin[12], A. Tomaradze[18], A. Toro[20], A. Tsaris[7], G. Vasileiadis[2], I. Vega[20], G. Voulgaris[2], N. K. Walford[4], T. Whitlatch[11], M. Williams[14], E. Wolin[11], T. Xiao[18], J. Zarling[10] and B. Zihlmann[11]

[1]*Arizona State University, Tempe, Arizona 85287, USA*
[2]*National and Kapodestrian University of Athens, 15771 Athens, Greece*
[3]*Carnegie Mellon University, Pittsburgh, Pennsylvania 15213, USA*
[4]*Catholic University of America, Washington, D.C. 20064, USA*
[5]*University of Connecticut, Storrs, Connecticut 06269, USA*
[6]*Florida International University, Miami, Florida 33199, USA*
[7]*Florida State University, Tallahassee, Florida 32306, USA*
[8]*University of Glasgow, Glasgow G12 8QQ, United Kingdom*
[9]*Institute for Theoretical and Experimental Physics, Moscow 117259, Russia*
[10]*Indiana University, Bloomington, Indiana 47405, USA*
[11]*Thomas Jefferson National Accelerator Facility, Newport News, Virginia 23606, USA*
[12]*National Research Nuclear University Moscow Engineering Physics Institute, Moscow 115409, Russia*
[13]*University of Massachusetts, Amherst, Massachusetts 01003, USA*
[14]*Massachusetts Institute of Technology, Cambridge, Massachusetts 02139, USA*
[15]*Norfolk State University, Norfolk, Virginia 23504, USA*
[16]*North Carolina A&T State University, Greensboro, North Carolina 27411, USA*

*XVIth International Conference on Hadron Spectroscopy*
AIP Conf. Proc. 1735, 020001-1–020001-8; doi: 10.1063/1.4949369
Published by AIP Publishing. 978-0-7354-1389-4/$30.00

[17]*University of North Carolina at Wilmington, Wilmington, North Carolina 28403, USA*
[18]*Northwestern University, Evanston, Illinois 60208, USA*
[19]*University of Regina, Regina, Saskatchewan, Canada S4S 0A2*
[20]*Universidad Técnica Federico Santa María, Casilla 110-V Valparaíso, Chile*
[21]*Yerevan Physics Institute, 375036 Yerevan, Armenia*

[a)]Corresponding author: cmeyer@cmu.edu

**Abstract.** The GlueX experiment at Jefferson Lab ran with its first commissioning beam in late 2014 and the spring of 2015. Data were collected on both plastic and liquid hydrogen targets, and much of the detector has been commissioned. All of the detector systems are now performing at or near design specifications and events are being fully reconstructed, including exclusive production of $\pi^0$, $\eta$ and $\omega$ mesons. Linearly-polarized photons were successfully produced through coherent bremsstrahlung and polarization transfer to the $\rho$ has been observed.

## INTRODUCTION

The GlueX Experiment [1] is a key element of the Jefferson Lab 12 GeV upgrade. The experiment is at the end of a new beamline from the Continuous Electron Beam Accelerator Facility (CEBAF) at Jefferson Lab, that will use 12 GeV electrons to deliver linearly-polarized photons to a new experimental area, Hall D. The primary physics goal of GlueX is to discover and study the properties of hybrid mesons–particles where the gluonic field contributes directly to the $J^{PC}$ quantum numbers of the mesons [2]. Lattice QCD calculations indicate that several of the nonets of these hybrid mesons have exotic quantum numbers, forbidden $J^{PC}$ for a simple fermion-antifermion system [3]. In addition, the expected masses for the lightest hybrids are well-matched to the energy and kinematics accessible to the GlueX experiment. Commissioning of the GlueX experiment started in late 2014 and continued through the spring of 2015. The first physics quality beam is expected in 2016. In this paper we report on the performance achieved both in calibrating and understanding the detector and present the measurement of the transfer of the photon's polarization to photo-produced $\rho$ mesons. The results from a few hours of running with polarized photons are consistent with older measurements [4, 5] and comparable in statistics to the older data.

## THE GLUEX EXPERIMENT

**The Hall D Photon Beam** The new Hall D facility has been designed as a photon-only hall, taking advantage of the 12 GeV electron beam from the upgraded CEBAF. The highest-energy electrons in the CEBAF accelerator are extracted and transported to the Hall D tagger hall. Here, they pass through a bremsstrahlung radiator, and then into a dipole magnet for tagging the energy of the scattered electrons. Those electrons not interacting in the bremsstrahlung radiator are deflected into an electron dump attached to the tagger hall. For the electrons producing a bremsstrahlung photon in the region between 25% and 98% of the primary electron beam energy, the scattered electrons are detected in a pair of tagger hodoscopes, thus tagging the energy of the photon. For 12 GeV electrons, the fine-grained *tagger microscope* (TAGM) has been placed to tag photons in the 8.2 GeV to 9.2 GeV range, with each microscope element spanning 10 MeV in energy. For both higher- and lower-energy photons, the *tagger hodoscope* (TAGH) tags photons using elements about 30 MeV wide. This is shown in the left-hand side of Figure 1.

Several different bremsstrahlung radiators are utilized in GlueX. The first are thin pieces of aluminum (1.5 $\mu m$, 10 $\mu m$ and 30 $\mu m$), while the second is a 20 $\mu m$ thick diamond[1] crystal. The diamond is aligned to produce coherent bremsstrahlung in the 8.4 GeV to 9.0 GeV range. These coherent photons are linearly polarized relative to the crystal axes in the diamond. The peak polarization is expected to be 40%, while the average polarization for 8.4 to 9.0 GeV photons is expected to be 36%. The diamond can be rotated to produce two perpendicular directions of linearly-polarized photons. The aluminum radiator produces a standard bremsstrahlung spectrum with the characteristic $1/E_\gamma$ fall off. Coherent bremsstrahlung photons are produced in the direction of the incident electrons, while incoherent bremsstrahlung photons are produced in a cone around that direction.

[1]During the spring 2015 running of GlueX at lower electron energies, 50 $\mu m$ and 100 $\mu m$ thick diamonds were utilized.

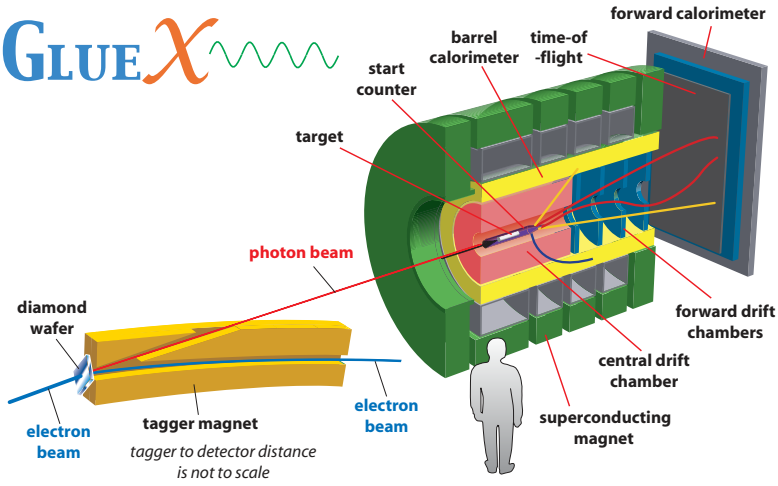


**FIGURE 1.** A schematic drawing of the Hall-D photon tagger and the GlueX detector at Jefferson Lab. See text for more information.

The photons travel through an 80 m long vacuum beamline before entering Hall D. Here, the off-axis photons are removed by passing the beam through a 3.4 mm diameter collimator[2] that has been instrumented around the hole with an *active collimator* [6] that provides fast feedback on the beam positioning. Photons passing through a primary collimator a secondary collimator, and then pass through a *triplet polarimeter* that is used to monitor the linear polarization. The photons then travel into a *pair spectrometer* system [7] that is used to monitor both the energy and intensity of the photon beam. The photons then travel into the GlueX detector, with some interacting in the liquid hydrogen physics target. The remainder pass into the photon beam dump at the back of Hall D.

Initial operation of the GlueX experiment will run at a beam intensity of $10^7$ photons per second in the coherent energy peak (8.2 GeV to 9.2 GeV), with the ultimate rate limit expected to be an order of magnitude higher. Operations during commissioning runs were at lower intensities.

**The GlueX Detector** The GlueX detector is azimuthally symmetric and nearly hermetic for both charged particles and photons, and is shown in the right-hand side of Figure 1. As noted above, the photon beam enters and is incident on a 30 cm long liquid hydrogen target which was successfully operated with the photon beam in the spring of 2015. The largest element of the GlueX detector is a solenoidal magnet, providing a magnetic field of about 2 T along the direction of the beam. Charged particles from the primary interaction first pass through the *start counter*, a 30-element scintillator detector that surrounds the hydrogen target and tapers towards the beamline in the forward direction. Light is detected using Hamamatsu Multi Pixel Photon Counters [8, 9] (silicon photomultipliers). The start counter measures a track timing with 300 ps resolution, which is sufficient to identify the bucket from the electron beam 499 MHz radio frequency (RF) structure from which the primary electron came. The start counter also provides information for track reconstruction and some particle identification capability through energy loss measurements.

Immediately surrounding the start counter is the *central drift chamber* (CDC) [10]. This detector is a 28 layer device based on straw-tube technology that includes both axial (12) and stereo (8 at 6° clockwise and 8 at 6° counter clockwise) layers with a total of 3522 straws. The CDC provides position measurements along the charged tracks with 150 $\mu m$ accuracy in the $r-\phi$ plane, and at the *mm* level along the beam axis by utilizing the stereo information. The detector also provides $dE/dx$ information for charged tracks and has good $\pi/p$ separation up to $p \sim 1$ GeV/$c$. The CDC is 150 cm long and has active elements between 10 cm and 59 cm radially.

Downstream of the CDC are the four packages of the *forward drift chamber* system (FDC) [11]. Each package is based on six layers of planar drift chambers with both anode and cathode readouts. The dual readout allows each layer to reconstruct a three-dimensional space point which is very helpful for tracking in the high-magnetic field environment. The FDC provides position measurements of charged tracks at the 200 $\mu m$ level as well as providing $dE/dx$ information for particle identification. The four detector packages are placed so as to allow charged particle

[2] During the spring 2015 run, a 5 mm diameter collimator was used.

track reconstruction down to a polar angle of about 1° from the beamline. Both drift chamber systems are read out using custom 125 MHz Flash ADC systems [12].

Surrounding the tracking devices inside the solenoid is the *barrel calorimeter* (BCAL) [13, 14, 15]. This is a lead-scintillating fiber calorimeter with readout on both the upstream and downstream layers. For particles entering normal to the calorimeter face, the calorimeter is 14.9 radiation lengths thick. The BCAL is sensitive to photons between polar angles of 12° and 160° and $\pi^0$ have been reconstructed using $\pi^0$ decay photons of energy below 100 MeV. The expected energy resolution is $\sigma E/E \approx 5.4\%/\sqrt{E}+2.3\%$ and the typical width of reconstructed $\pi^0$ for GlueX reactions is about 9 MeV. Due to its proximity to the solenoidal field, the BCAL is read out using the same Hamamatsu Multi Pixel Photon Counters as in the start counter [9]. The BCAL is read out using both 250 MHz custom Flash ADCs as well as 60 *ps* TDCs. The timing information is used to provide time-of-flight information for particles interacting in the BCAL, and is used in the global particle identification methods for both charged particles and photons.

The second calorimeter system in GlueX, the *forward calorimeter* (FCAL), is located downstream of the solenoidal magnet [16]. This consists of 2800 lead-glass crystals, each 45 cm long (14.5 radiation lengths). The crystals are stacked such that the active area of the FCAL is circular, and spans polar angles from 12° down to 1°. The FCAL is sensitive to photons of $E_\gamma \geq 100$ MeV, which is well-matched to the kinematics of GlueX. The energy resolution of the FCAL is expected to be $\sigma_E/E \approx 5.6\%/\sqrt{E} + 3.5\%$.

Upstream of the FCAL is the *time-of-flight wall* (TOF), which consists of two layers of 2.5 cm thick scintillator bars with readout using photomultiplier tubes on both ends of the detector. Signals from the TOF are processed in both high-resolution TDCs and Flash ADCs to provide both timing and energy-loss information. The timing resolution of the TOF system is 100 ps, providing particle identification for polar angles from 12° down to 1°.

## DETECTOR PERFORMANCE

During the GlueX commissioning runs in late 2014 and spring 2015, nearly two billion triggered events were recorded under a variety of trigger, detector, and magnetic field configurations. In addition, triggering on cosmic events has been ongoing since the summer of 2014. All of these data have been used to align and calibrate the detector, as well as assess the overall performance of the detector.

**The Photon Beam** The TAGM and TAGH systems are used to determine the energy of the beam photon. The combined system is checked using the pair spectrometer, which uses a convertor to produce an $e^+e^-$ pair from a primary photon, and then detects the electrons and positrons in coincidence. A special trigger looks for events in the pair spectrometer and then reads out the pair spectrometer system together with TAGH and TAGM. This allows us to determine and monitor the energy calibration of the tagger system. Energy resolutions of both the TAGH and TAGM systems are given by detector geometry and alignment and design resolution has been reached.

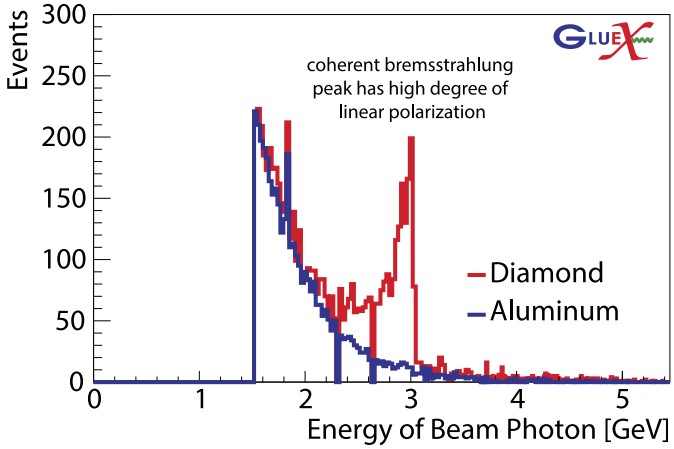


**FIGURE 2.** The number of events as a function of photon beam energy for the aluminum radiator (blue), and a thin diamond radiator (red). The $1/E_\gamma$ intensity fall off is clearly seen for the aluminum radiator, while the coherent enhancement is clearly seen for the diamond radiator.

In addition to the photon energy, the linear polarization of the photon beam is also important. This aspect of the beam has been commissioned using a 5.5 GeV electron beam and a 50 $\mu m$ thick diamond radiator. Figure 2 shows the energy spectrum of photons for an amorphous radiator and the diamond radiator. The expected $1/E_\gamma$ spectrum is seen for the amorphous radiator, while the coherent enhancement at about 3 GeV energy is observed with the aligned diamond radiator. Using the shape of the coherent peak, the linear polarization is calculated to be 60% at the coherent edge and an average of 50% over photon energies in the 2.5 to 3.0 GeV range. An independent measurement using the triplet polarimeter yielded a consistent result. Finally, as discussed later, measurement of the $\rho$ polarization also yielded a photon polarization consistent with the other measurements.

**The GlueX Detector** Listing detectors in the same order as above, calibration of the start counter has achieved a resolution better than the 300 ps design resolution and is sufficient to identify the RF beam bucket of the primary electron. The CDC has achieved a resolution of 200 $\mu m$ prior to correcting for straw deformations. Ongoing work on these latter corrections shows that the resolution will likely be better than the design goal of 150 $\mu m$. For the FDC, the cathode resolution has reached the design value of 200 $\mu m$, while the anode resolutions have reached 150 $\mu m$, exceeding design specifications. For events with multiple tracks from the same vertex, the vertex positions were reconstructed with a resolution 3-4 mm averaged over all tracks. For the calorimeters, energy calibration procedures rely on optimizing the reconstructed $\pi^0$ mass by adjusting appropriate constants. While the methods have been shown to work, the sizable data set needed to carry out the calibration is not yet available. An example of current calorimeter performance is shown in the left-hand plot in Figure 3, where both the $\pi^0$ and $\eta$ are reconstructed from their two photon decays for events from the exclusive final state $\gamma p \to p\gamma\gamma$. Currently, a $\pi^0$ width better than 9 MeV has been achieved using photons detected in the BCAL and in the FCAL. In the right-hand plot is shown the $\pi^+\pi^-\pi^0$ invariant mass for events from the exclusive final state $\gamma p \to p\pi^+\pi^-\gamma\gamma$. A clear signal for the $\omega \to \pi^+\pi^-\pi^0$ is observed, where the width of the $\omega$ peak is found to be well-described by a Breit-Wigner peak, with the 8.49 MeV width of the $\omega$ convoluted with a Gaussian with a resolution of $\sigma$ = 31.5 MeV.

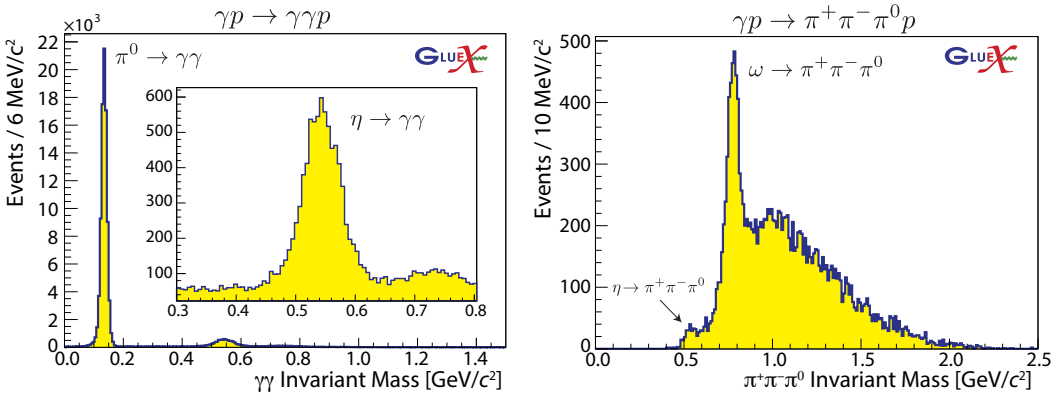


**FIGURE 3.** (Left) The $\pi^0$ and $\eta$ masses as determined from a pair of photons from $\gamma p \to p\gamma\gamma$ events. The lower-left image shows the full invariant mass range where the $\pi^0$ and $\eta$ peaks are visible. The insert on the upper right zooms in on the $\eta$ peak. (Right) The $\pi^+\pi^-\pi^0$ invariant mass from $\gamma p \to p\pi^+\pi^-\gamma\gamma$ events where $m_{\gamma\gamma}$ is consistent with the mass of the $\pi^0$. In both reactions, the detected photons can be in both the BCAL and the FCAL.

The TOF system has also achieved 100 ps timing resolution for charged particles that are detected in both planes of the system. One of the primary uses of the TOF is to help with particle identification. This process involves not only a flight time, as determined from the RF beam bunch and the TOF, but also the path length and momentum of the charged particle as determined by the CDC and FDC systems. Figure 4 shows one way to evaluate particle identification, where the calculated $\beta$ of a charged particle is plotted against its momentum. The figure shows positively charged particles, and clear bands are seen for $e^+$, $\pi^+$, $K^+$, and protons, with clear proton identification up to 3 GeV/$c$ and $\pi/K$ separation up to about 2 GeV/$c$. For charged particles traversing the CDC, energy-loss measurements ($dE/dx$) are made concurrently with each position measurement. The right hand image in Figure 4 shows the measured $dE/dx$ for positively-charged particles as a function the particle's momentum. Clear $\pi/p$ separation is evident up to about 1 GeV/$c$.

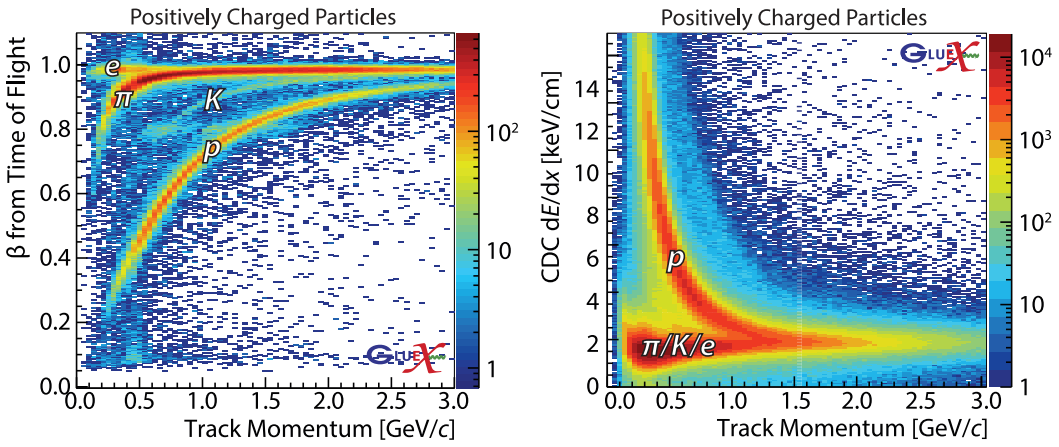


**FIGURE 4.** For positively charged particles: (Left) the $\beta$ as determined from both time-of-flight and path-length measurements in the detector versus the reconstructed particle momentum and (Right) energy loss $dE/dx$ in the CDC as a function of reconstructed particle momentum.

## POLARIZATION TRANSFER TO THE $\rho$ MESON

For vector meson photoproduction using linearly polarized photons, one of the observables that can be measured is the beam asymmetry, $\Sigma$, which can be interpreted as the percentage transfer of the linear polarization of the photon to the vector meson. If the spin-density matrix elements of the vector meson can be measured [17], then $\Sigma$ can be written directly in terms of them.

$$\Sigma \quad = \quad \frac{\rho^1_{11} + \rho^1_{1-1}}{\rho^0_{11} + \rho^0_{1-1}} \, ,$$

The measurement of the $\rho^1_{ij}$ requires linearly polarized photons. Alternatively, the polarization transfer can be approximately determined by measuring the angular distribution of the vector meson decay through

$$\frac{d\sigma}{d\psi} \quad \propto \quad 1 + P\,\Sigma\,\cos 2\psi \, ,$$

where $P$ is the linear polarization of the photon beam and $\psi$ is the azimuthal angle between the photon polarization vector and the decay plane of the vector meson. This angle is illustrated in the left-hand side of Figure 5. For the case of the $\rho$ meson, $\Sigma$ has been measured to be close to unity for the photon energies of interest [5, 18, 19].

Using a 5.5 GeV electron beam and a 50 $\mu m$ thick diamond radiator, linearly polarized photons were produced in the 2.5 to 3.0 GeV energy range. From all the collected events, we selected exclusive $\gamma p \rightarrow \pi^+\pi^- p$ events utilizing many of the detector systems described in the previous sections. Charged particle tracks for the proton, $\pi^+$ and $\pi^-$ were reconstructed using the CDC and FDC. For proton tracks we required a large $dE/dx$ measured in the CDC, which provides good separation from $\pi^+$ tracks up to $p \sim 1$ GeV/c (see the right-hand image in Figure 4). As the tagged, initial-state photon energy and the final-state particle momenta are all independently measured, the event kinematics are over-constrained. Thus, momentum conservation was enforced by utilizing the magnitude of the difference between the initial and final state 4-momenta, requiring $|(p_{final} - p_{initial})^2| < 0.02\,\mathrm{GeV}^2/\mathrm{c}^4$. The resulting $\pi^+\pi^-$ invariant mass distribution is shown in Figure 6. For determining the polarization transfer to the $\rho$ we selected $\pi^+\pi^-$ candidates with $0.60 < M_{\pi^+\pi^-} < 0.95\,\mathrm{GeV}/\mathrm{c}^2$, and beam photons with $2.5 < E_\gamma < 3.0$ GeV, where the coherent bremsstrahlung is enhanced (see Fig. 2).

The measured decay distribution for both unpolarized and linearly polarized photons is shown in the right-hand side of Figure 5. For the case of the aluminum radiator (unpolarized photons), the angular distribution is uniform, while for the diamond radiator (linearly polarized photons), there is a clear $\cos 2\psi$ dependence. These azimuthal decay distributions are not corrected for acceptance. However these corrections should be small due to the azimuthal symmetry of the GlueX detector, which is nicely demonstrated by the uniform distribution in the case of the aluminum

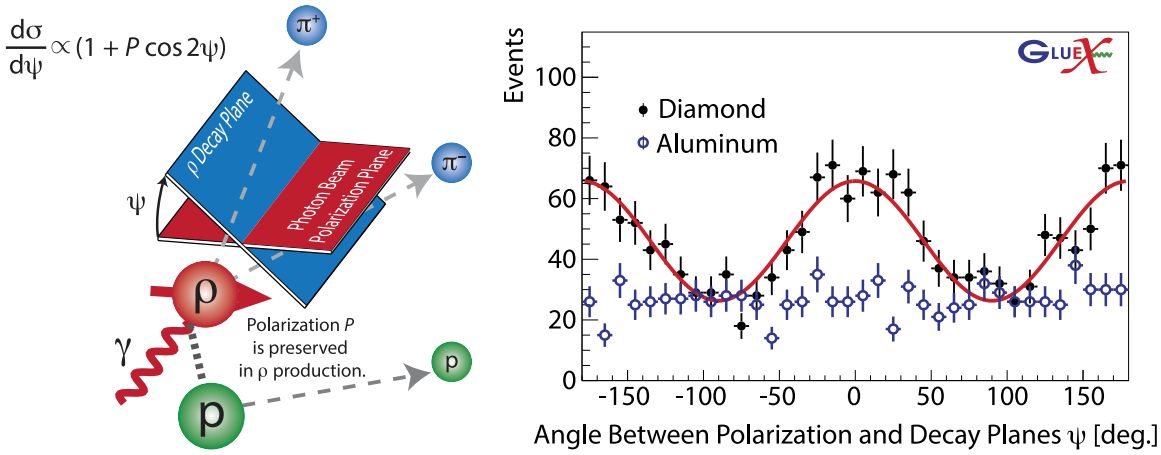


**FIGURE 5.** The decay angular distribution for the $\rho$ meson for linearly polarized photons (red curve on solid black markers) and for unpolarized photons (blue open markers).

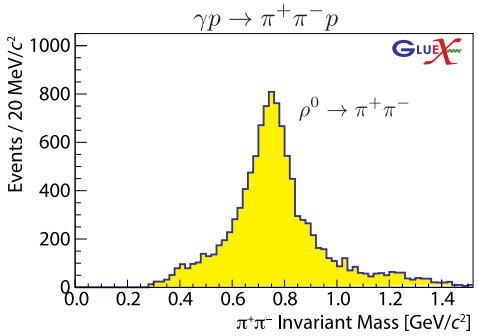


**FIGURE 6.** The reconstructed $\pi^+\pi^-$ invariant mass for events from the exclusive reaction $\gamma p \to p\pi^+\pi^-$.

radiator. As noted earlier, taking the value of $\Sigma$ from earlier measurements one can determine the linear polarization of the photon beam, $P$, extracted from a fit to this angular distribution is consistent with the photon polarization determined from the shape of the coherent peak as described earlier. The number of events in Reference [5] is similar to what was obtained in GlueX in a few hours of low-intensity commissioning running. This observation of the polarization transfer to the $\rho$ provides clear evidence that with full intensity, significant new physics results from GlueX will be possible.

## SUMMARY

Commissioning of the Hall D beamline and the GlueX experiment at Jefferson Lab is well underway. Calibrations of the detector systems are in an advanced state, with many systems at, or exceeding, design specifications. All systems are within 30 % of design specifications, and once sufficient data are obtained to complete calibrations, all are expected to reach design specifications. While the hardware trigger allowed for substantial data taking, improvements are still being made. While early commissioning data ran with a very-large data footprint to enable studies of the acquisition and data transfers, the experiment will be implementing the final compact formats in late 2015 and 2016, and rates are expected to reach design expectations. Offline analysis of data has also evolved rapidly, and a smooth system is now in place to speedily process production data and produce a very compact analysis format. These later data have been used to extract physics from GlueX, as evidenced by the measured decay distribution of the $\rho$.

## ACKNOWLEDGMENTS

The authors thank the staff and administration of the Thomas Jefferson National Accelerator Facility who made this experiment possible. This work was supported in part by the U.S. Department of Energy (under grants DE-FG02-87ER40315, DE-FG02-92ER40735, DE-FG02-94ER40818 , DE-SC0010497, DE-FG02-87ER40344, and DE-FG02-05ER41374); the National Science Foundation (under grants PHY-1207857, PHY-1508238, PHY-1306418, PHY-1206043, PHY-1506303, PHY-1507208, and PHY-1306737); the Natural Sciences and Engineering Research Council of Canada (NSERC) (under grant numbers SAPJ-326516 and SAPIN-105851-2011), and the UK Science and Technology Facilities Council (STFC) (under grant number ST/L005719/1). This material is based upon work supported by the U.S. Department of Energy, Office of Science, Office of Nuclear Physics under contract DE-AC05-06OR23177.

## REFERENCES

[1] The GlueX Collaboration, The GlueX Experiment in Hall D, 2010, Presentation to JLab PAC 36, http://www.gluex.org/docs/pac36_update.pdf.
[2] C. A. Meyer and E. S. Swanson, Prog. Part. Nucl. Phys. **82**, 21–58 (2015).
[3] J. J. Dudek, R. G. Edwards, P. Guo, and C. E. Thomas (Hadron Spectrum), Phys. Rev. **D88**, p. 094505 (2013).
[4] L. Criegee *et al.*, Phys. Lett. **B28**, 282–286 (1968).
[5] J. Ballam *et al.*, Phys. Rev. Lett. **24**, 960–963 (1970).
[6] G. Miller and D. Walz, Nucl. Instrum. Methods **117**, p. 33 (1974).
[7] F. Barbosa, C. Hutton, A. Sitnikov, A. Somov, S. Somov, and I. Tolstukhin, Nucl. Instrum. Methods **A795**, 376–380 (2015).
[8] F. Barbosa, J. McKisson, J. McKisson, Y. Qiang, E. Smith, and C. Zorn, Nucl. Instrum. Methods **A695**, 100–104 (2012).
[9] O. Soto, R. Rojas, S. Kuleshov, H. Hakobyan, A. Toro, and W. Brooks, Nucl. Instrum. Methods **A732**, 431–436 (2013).
[10] Y. Van Haarlem, C. A. Meyer, F. Barbosa, B. Dey, D. Lawrence, V. Razmyslovich, E. S. Smith, G. Visser, T. Whitlatch, G. Wilkin, and B. Zihlmann, Nucl. Instrum. Methods **A622**, p. 142 (2010).
[11] V. V. Berdnikov, S. V. Somov, L. Pentchev, and B. Zihlmann, Instrum. Exp. Tech. **58**, p. 25 (2015).
[12] G. Visser, D. Abbot, F. Barbosa, C. Cuevas, H. Dong, E. Jastrzembski, B. Moffit, and B. Raydo, Nuclear Science Symposium Conference Record (NSS/MIC) 777–781 (2010).
[13] B. Leverington *et al.*, Nucl. Instrum. Methods **A596**, p. 327 (2008).
[14] Z. Papandreou, B. Leverington, and G. Lolos, Nucl. Instrum. Methods **A596**, p. 338 (2008).
[15] A. Baulin *et al.*, Nucl. Instrum. Methods **A715**, 48–55 (2013).
[16] K. Moriya *et al.*, Nucl. Instrum. Methods **A726**, 60–66 (2013).
[17] K. Schilling, P. Seyboth, and G. Wolf, Nucl. Phys. **B15**, 397–412 (1970).
[18] J. Ballam *et al.*, Phys. Rev. **D5**, p. 545 (1972).
[19] J. Ballam *et al.*, Phys. Rev. **D7**, 3150–3177 (1973).
[20] J. J. Dudek, R. G. Edwards, B. Joo, M. J. Peardon, D. G. Richards, and C. E. Thomas, Phys. Rev. **D83**, p. 111502 (2011).